The Origin of Metal Loading Heterogeneities in Pt/Zeolite Y Bifunctional Catalysts

Lars I. van der Wal,[a] Krijn P. de Jong,[a] and Jovana Zečević*[a]

Preparing catalysts with highly dispersed metal nanoparticles and narrow particle size distribution has been in the focus of numerous studies. Besides size and size distribution, the location of metal nanoparticles within and local metal loading of the support can have significant impact on catalytic performance. This study revealed that great variations in Pt loading between individual Pt/zeolite Y crystals occurred irrespective of the metal deposition method, namely ion-exchange (IE) or incipient wetness impregnation (IWI). The variation in Pt loading was found to be directly related to different Si/Al ratios of individual zeolite crystals. Results indicate that this Si/Al variation was likely induced by post-synthesis treatments, commonly performed to introduce mesoporosity. In view of the great importance of zeolite-based catalysts for oil refining, understanding the origin of such metal loading heterogeneities may lead to further improvement of zeolite-based catalytic performance.

Introduction

Bifunctional zeolite-supported metal catalysts are highly important for industrial oil-refining processes such as hydroisomerization.[1–6] Their bifunctionality originates from the presence of both metal sites, which perform (de)hydrogenation of hydrocarbons, and zeolite acid sites which perform isomerization/cracking of the dehydrogenated hydrocarbon species. To achieve high activity, selectivity and stability of the catalysts, various parameters should be optimized, including the metal to acid site ratio,[7] high dispersion of the metal nanoparticles[8] and a homogeneous distribution of the metal on the support.[9] The latter maximizes the distance between metal particles which is beneficial for catalyst stability,[9] while high dispersion increases catalyst activity.[10–15] In addition, the presence of mesopores (2–50 nm diameter) in zeolites is favorable, as zeolite micropores (~1 nm diameter) can cause diffusion limitations.

In the oil refining industry, zeolite Y is a leading catalyst for cracking and hydroisomerization reactions.[16] This zeolite has a crystalline structure with a Si/Al ratio of 2.6 and a well-defined 3D micropore network, with micropore supercages of 1.2 nm in diameter and entrances of 0.6 nm. Due to the size of micro-

pores, mass transfer limitations may occur and, as a result, undesired reactions can take place including secondary cracking and the formation of coke.[17–20] In order to overcome this problem, zeolite Y is commonly steamed and acid leached to obtain so-called ultra-stable Y zeolite (USY), which introduces mesopores, enhances the zeolite's hydrothermal stability and reduces the number of Al sites to a Si/Al ratio of 30.[20–25] The number of Al sites relates to the number of acid sites when protons are used to compensate for charge caused by Al^{3+} replacing Si^{4+} in SiO_2 tetrahedra building blocks of the zeolite structure.

The metal function of the bifunctional zeolite catalysts is typically introduced via incipient wetness impregnation (IWI) or ion-exchange (IE). In IWI, the pore volume of the zeolite support is filled with the same or slightly lower volume of metal precursor solution.[26] In IE, the zeolite support is dispersed in an excess of metal precursor solution, upon which the charge compensating cations (e.g. protons) present in the zeolite support are exchanged for the metal precursor cations.[26]

Irrespective of the metal loading method, heterogeneities in metal distribution can occur, especially when metal loading is performed on millimeter-sized catalyst bodies.[27] Frequently inhomogeneous egg-shell or egg-yolk metal distributions are obtained, depending on the chemical nature of metal ions and the support, and thus on the rate of adsorption and rate of diffusion of metal ions through the catalyst body.[26,28] Likewise, heterogeneities were observed between micrometer-sized granules when these were used as catalyst support.[29,30] It was shown that the drying procedure had a large influence on metal distribution. When static air drying was used, the amount of metal in the granules depended on the position of the granule in the static catalyst bed. However, when fluidized bed drying was used, a homogeneous metal distribution between the granules was achieved.[30]

Apart from heterogeneities in metal distribution at millimeter and micrometer scale, which are relatively well studied and understood till now, an earlier study revealed that metal

[a] L. I. van der Wal, Prof. K. P. de Jong, Dr. J. Zečević
Inorganic Chemistry and Catalysis
Debye Institute for Nanomaterials Science
Utrecht University
Universiteitsweg 99, 3584 CG, Utrecht (The Netherlands)
E-mail: j.zecevic@uu.nl

distribution heterogeneities can occur even on the nanometer scale.[31] It has been shown that individual zeolite Y crystals (300–500 nm in size) within a sample can have very different Pt metal loadings when prepared by IWI. For the nominal 1 wt% Pt metal loading in a bulk catalyst, the Pt loading varied from 0.2 wt% Pt to 7 wt% Pt between individual zeolite crystals. This surprising observation was made by combining electron tomography (3D transmission electron microscopy) and 3D-image segmentation and quantification of individual zeolite crystals and Pt particles within. Since no morphological differences between crystals (e.g. mesoporosity, zeolite crystal size) could explain the loading heterogeneity, it was argued that the origin of the heterogeneity might lie in different chemical composition, that is different Si/Al ratios between zeolite crystals and thus variation in available sites for Pt ion exchange/adsorption.

As mentioned above, many of the parameters, such as metal to acid site ratio, can have great impact on catalyst performance.[14,15] Even if these parameters are satisfied on bulk scale in the catalyst, the presence of large heterogeneities on nanometer scale can lead to differences in performance between crystals, leading to a broadening of the product distribution and non-optimal use of the metal catalyst. It is therefore of importance to elucidate the origin of the nanoscale heterogeneities in metal loading so that the metal deposition techniques can be optimized in order to homogeneously distribute the metal and to potentially even reduce metal loading.[31,32]

In this research we focused on determining the local zeolite Y chemical composition simultaneously with the local Pt metal loading in order to elucidate whether variation in Si/Al ratio between zeolite crystals is the origin of the Pt loading heterogeneities. For this purpose, elemental analysis of single zeolite crystals was performed using transmission electron microscopy-based energy dispersive X-ray (EDX) spectroscopy. The results unambiguously point to the correlation between the Al content of a zeolite Y crystal and the Pt loading of that crystal. Furthermore, we extended the research on bifunctional Pt-zeolite Y catalysts obtained both via IE as well as IWI to investigate the influence of preparation method, along with preparing catalysts with different bulk Pt loadings to study the impact of bulk loading on loading heterogeneities at nanometer scale.

Results and Discussion

The set of Pt-zeolite Y samples with different nominal Pt loading (1–3 wt%) was prepared using steamed and acid leached mesoporous zeolite Y (CBV760, Zeolyst) and $Pt(NH_3)_4(NO_3)_2$ aqueous solution following either IE or IWI method as described in detail in the Experimental Section. EDX analysis using both scanning and transmission electron microscopy (SEM and TEM) was performed to determine the average platinum weight loading of the synthesized Pt-zeolite Y catalysts (Table 1). For this analysis, regions of tens of micrometers in size containing thousands of Pt-zeolite Y crystals were subjected to electron

Table 1. Platinum weight loading for the IE and IWI prepared samples as determined with TEM-EDX, SEM-EDX and ICP-OES.

Sample	Pt[a] [wt%]	Pt[b] [wt%]	Average[c] [wt%]	Pt[d] [wt%]
IE-1.3	1.4	1.1	1.3	1.6
IE-1.8	1.7	1.8	1.8	2.1
IE-1.9	1.9	1.8	1.9	2.1
IE-2.4	2.3	2.5	2.4	3.0
IWI-0.9	0.8	0.9	0.9	1.1
IWI-1.4	1.2	1.5	1.4	1.7
IWI-1.6	1.2	1.9	1.6	1.9
IWI-2.8	3.1	2.4	2.8	2.6

[a] As determined with bulk TEM-EDX. [b] As determined with SEM-EDX. [c] The average of TEM-EDX and SEM-EDX measurements. [d] As determined with ICP-OES.

beam illumination. Negligible differences in Pt loading derived by SEM-EDX and TEM-EDX were observed, and the average between the two values was used for the nomenclature, e.g. IE-1.3 stands for an ion-exchange prepared sample with an average Pt weight loading of 1.3 percent. ICP-OES measurements were also performed to determine the bulk Pt loading (Table 1), which pointed to the same trend in Pt loading between the catalysts but gave higher (15–20%) Pt loadings than those detected by EDX measurements. Despite underestimation of Pt loading by electron microscopy techniques, the obtained results confirm that EDX is sensitive enough to detect differences in Pt loading even at such low Pt content.

Local information on Pt size and distribution across zeolite crystals was derived from scanning transmission electron microscopy (STEM) imaging. Particle size analysis was carried out, for which >500 metal nanoparticles were measured. Representative high-angle annular dark-field (HAADF) STEM images of the samples as well as Pt particle size histograms are shown in Figure 1. It can be seen that in all the samples the majority of the Pt particles has a diameter of 0.5–2 nm, with a small fraction of larger particles (2–10 nm) occurring particularly in the samples with higher Pt loadings. In exceptional cases, also particles in the range of 20–40 nm were observed, but are not shown in particle size histograms. In order to investigate whether the amount of these large Pt particles was significant, as they can be easily omitted in local TEM analysis, XRD and H_2-chemisorption measurements were performed. For all samples a very small peak was observed at a diffraction angle of 47°,

Table 2. Average particle sizes as determined with TEM and H_2-chemisorption for the prepared samples. Here d_N is the number averaged particle size, whereas d_S is the surface averaged particle size.

Sample	d_N[a] [nm]	d_S[a] [nm]	d_S[b] [nm]
IE-1.3	1.5 ± 1.0	1.8 ± 1.0	1.2
IE-1.8	1.7 ± 1.0	1.9 ± 1.0	1.0
IE-1.9	1.9 ± 1.7	2.5 ± 1.8	1.6
IE-2.4	1.9 ± 1.7	2.6 ± 1.9	1.1
IWI-0.9	1.7 ± 1.3	2.1 ± 1.3	0.9
IWI-1.4	1.7 ± 1.1	2.1 ± 1.2	1.5
IWI-1.6	1.8 ± 1.3	2.2 ± 1.3	1.2
IWI-2.8	2.0 ± 1.8	2.7 ± 1.9	1.7

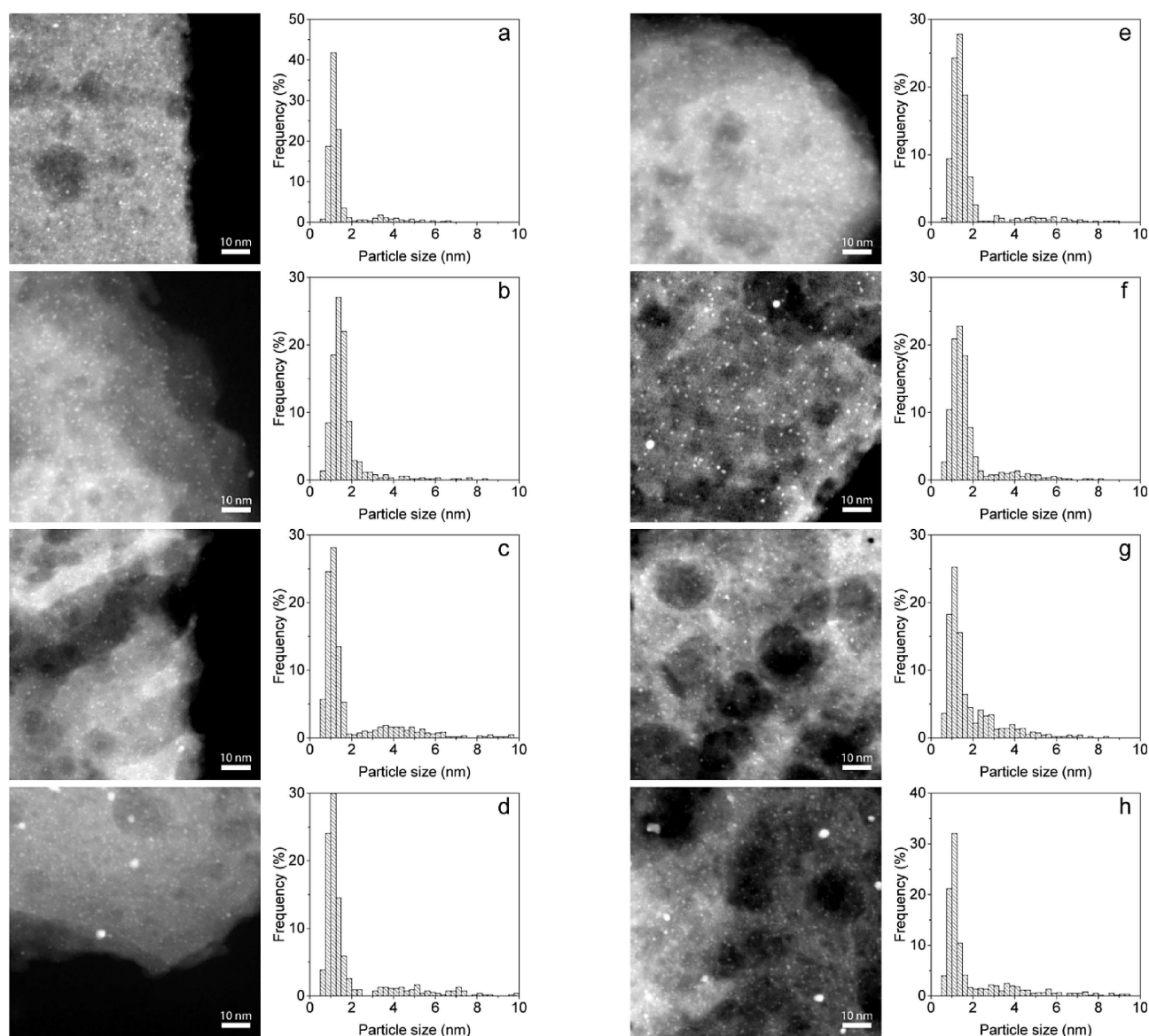[a] As determined with TEM. [b] As determined with H_2-chemisorption.

Figure 1. HAADF-STEM images and number averaged particle size histograms of (a) IE-1.3, (b) IE-1.8, (c) IE-1.9, (d) IE-2.4, (e) IWI-0.9, (f) IWI-1.4, (g) IWI-1.6 and (h) IWI-2.8 samples.

which is typical for metallic Pt (Supporting Information, Figure S1). For IWI-1.4, however, a somewhat larger peak was observed at this diffraction angle, suggesting that larger Pt particles could be present in this sample. In order to verify the contribution of the larger particles to the average particle size, H_2-chemisorption measurements were performed (Table 2). The results showed that the surface averaged particle size determined with H_2-chemisorption was lower than the one determined by TEM, but still within 1–2 nm range for all the samples. It should be mentioned that for the determination of the particle size with H_2-chemisorption several assumptions were made, including that Pt formed (hemi)spherical particles and that the H:Pt$_s$ stoichiometry was 1. The H:Pt$_s$ stoichiometry can, however, be larger than 1,[33] and thus lead to underestimation of Pt particle sizes. Even with this taken into account, the values

obtained by H_2-chemisorption were in a size range of those obtained by TEM, confirming that the large particles did not greatly contribute to the average particle size and that the majority of Pt particles are 1–2 nm in diameter in all catalysts.

Visual inspection of STEM images already suggests the difference in Pt loading between zeolite crystals, in line with the observations of the earlier study using electron tomography.[31] Furthermore, this difference seems to be irrespective of the method used for preparation and of the nominal Pt loading, as demonstrated in Figure 2 showing IE-1.3 and IWI-0.9 samples. To quantitatively assess the Pt loading of individual zeolite crystals, and to try to correlate it with chemical composition of the zeolite crystals, an EDX study was performed in TEM imaging mode. Analysis was performed on 20 individual zeolite crystals for each sample, whereby individual zeolite crystals
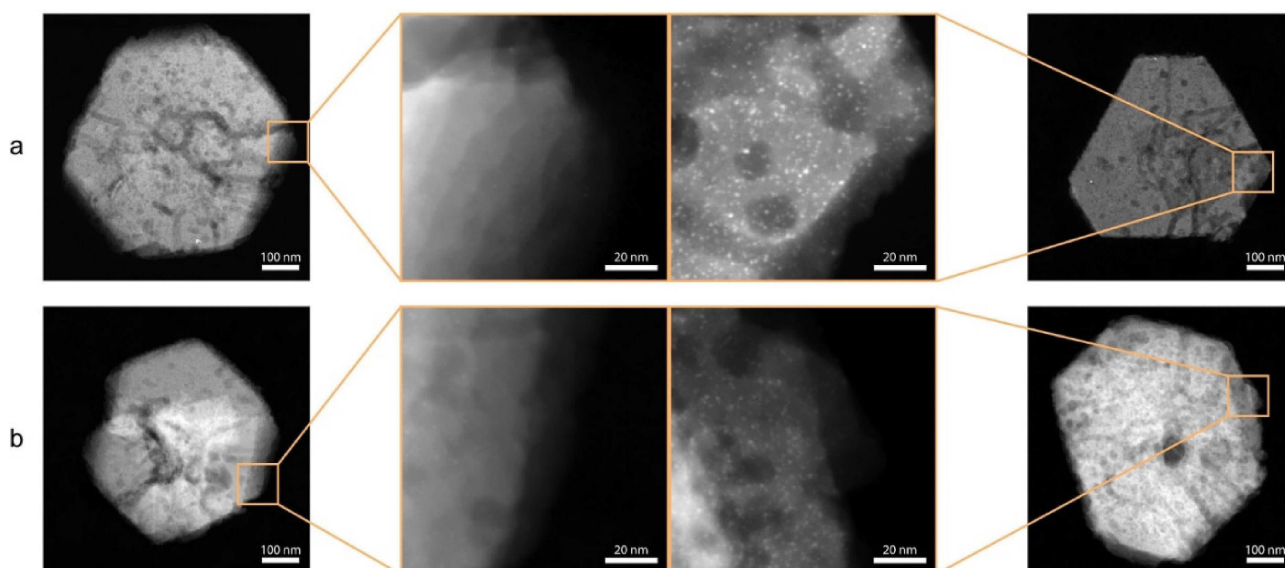
Figure 2. Pt-loading heterogeneities observed within the samples for (a) IE-1.3 (b) IWI-0.9. The images on the left represent crystals with low Pt loading, whereas the images on the right represent crystals with high Pt loading. Similar loading heterogeneities were observed in all synthesized samples.

were illuminated with the electron beam in such a way that no other zeolite crystal or material was exposed to electron beam irradiation apart from carbon foil of the TEM grid. Corresponding X-ray emissions were collected using a Super-X^{TM} EDX detector (FEI). The EDX spectra were analyzed and quantified to extract atomic ratios of elements present in the samples, namely Si, Al, O and Pt. The quantification results are shown in Figure 3, where the Pt and Al content are presented relative to the Si content.

The most noteworthy feature that can be observed in Figure 3 is that, in all samples, Pt content increases as the Al/(Si +Al) ratio increases. This indicates that the platinum loading strongly depended on the amount of Al present in the zeolite crystal. Importantly, this dependence was observed not only for the IE-prepared samples (Figure 3a), where number of Al sites available for the Pt ion exchange is crucial, but also for the IWI-prepared samples (Figure 3b). Although the IWI method is based on the pore filling and is methodologically independent on chemical interaction, the results suggested that ion adsorption/exchange also takes place during IWI. Furthermore, the Pt—Al dependence was observed irrespective of the nominal Pt loading, which was varied between 1 and 3 wt% for both IE and IWI samples. Therefore, differences in Si/Al ratio between the individual crystals of the zeolite support seem to be the leading cause for heterogeneities in Pt loading observed here and in the earlier study.

Another important characteristic of the plots is the degree of correlation between the data points, expressed by the correlation coefficient R^2_{adj}. The plots were fitted with a linear function ($y = a + bx$), since the Al/(Si +Al) ratio is assumed to linearly scale with the amount of acid sites and thereby Pt content. Whereas a R^2_{adj} of 1.0 represents a perfect correlation, a R^2_{adj} of approximately 0 indicates no correlation between the data points. While the correlation coefficient R^2_{adj} for the IE
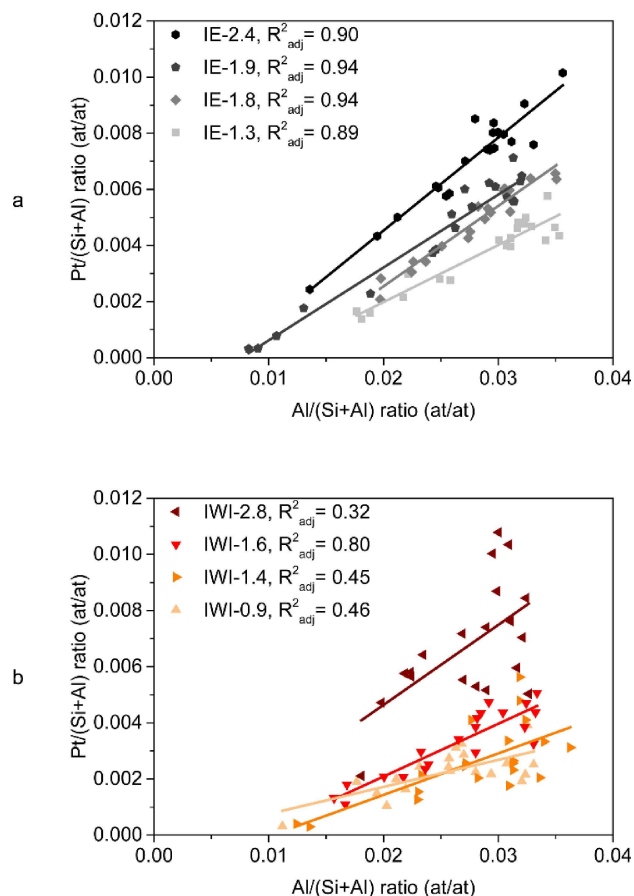

Figure 3. Quantitative EDX analysis of the individual zeolite crystals (data points). Graphs showing Pt loading (Pt/(Si +Al) ratio) as function of the Al/(Si +Al) ratio for (a) IE prepared samples and (b) IWI prepared samples with different bulk Pt loadings.

prepared samples is noticeably high (~0.9), that of the IWI samples is rather low (~0.5). This highlights the fact that the IE method is driven by and strongly depends on the amount of Al, and thus the number of zeolite protons for the exchange with platinum ions. For the IWI method, on the other hand, the heterogeneities in Pt loading cannot solely be ascribed to the heterogeneity in Al content between the crystals. Here, most likely other factors also contribute to the heterogeneity, such as insufficient mixing during IWI and depletion of Pt from the precursor solution by crystals that first come in contact with the solution.

Differences between IE and IWI methods are also reflected in slope heights, with IE samples showing higher slopes than samples prepared via IWI (Figure 3, Supporting Information Table S1). Lower slopes in IWI, and thus lower amount of Pt per zeolite crystal, indicate that a portion of Pt detected by bulk analysis is not residing inside zeolite crystals. This is likely a result of platinum precursor solution filling also the inter-particle porosity of zeolite powder during IWI, which could ultimately lead to formation of large Pt particles outside of the zeolite crystals. In fact, Figure 1 shows that Pt particles larger than 1–2 nm occur more frequently in IWI samples. Since the samples are ground and sonicated in an ultrasonic bath during TEM sample preparation, it is possible that some of the larger Pt particles residing on the zeolite surface detached and could not be detected during EDX analysis of individual zeolite crystals.

It can also be observed that the fitted lines do not go through the origin, but a positive value of the Al/(Si+Al) ratio (Figure 3) is observed. One of the explanations could be the presence of extra-framework aluminum which does not contribute to Pt adsorption. As described in the last paragraph, extra-framework aluminum is created during the steaming, and it is subsequently leached during the acid treatment of parent zeolite Y. From a number of ^{27}Al MAS NMR measurements reported in literature it can be seen that extra-framework aluminum is still present and ranges from 16.7–25.0% of the total Al content in commercially available, steamed and acid leached, zeolite Y (CBV760) used in this study.[35–37] Taking into account the Si/Al ratio, this corresponds to a Al/(Si+Al) ratio ranging from 0.005–0.010, which coincides well with the intercept of the Al/(Si+Al) observed in our study. However, although EDX is not suited to distinguish between differently coordinated aluminum, one would expect for Al EDX signal to be stronger along the mesopore walls in case extra-framework Al was still present. Such extra-framework Al deposits in the mesopores of pre-acid leached zeolite Y (CBV400) were earlier detected with electron tomography, while subsequent acid leaching seemed to have successfully removed it.[25] As can be seen in Figure 4 (bottom row), no significant Al deposition was detected on the mesopore walls or outer surface of the steamed and acid leached zeolite Y. Furthermore, during EDX analysis, clusters of several hundred nanometers to micro-meters, containing mostly Al, could be observed next to zeolite crystals (Supporting Information, Figure S2). This indicates that the extra-framework aluminum residing inside zeolite crystals is likely much lower than bulk reported values and therefore cannot fully explain the observed Al/(Si+Al) offset.
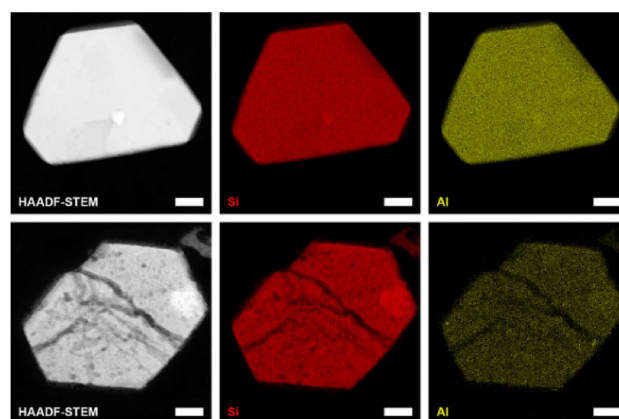

Figure 4. HAADF-STEM and EDX maps of pristine zeolite Y (top row) and steamed and acid-leached zeolite Y (bottom row). The left column (white) shows the HAADF-STEM image. The middle column shows the Si EDX map (red) and the right column shows the Al EDX map (yellow). Scale bars are 100 nm.

Another explanation for the observed Al/(Si+Al) offset could be that there is a minimum number of Al atoms needed for two Al sites to be close enough to participate in accommodating one Pt^{2+} ion. Interestingly, the data obtained here suggests that this threshold is at an Si/Al ratio of approximately 100, which corresponds to roughly 0.5 Al sites per zeolite supercage assuming that Al is homogeneously distributed throughout the lattice. For accommodating a divalent cation it is typically assumed that two Al sites should be at a "visible distance" within the zeolite cage.[34] Our result thus indicates that either Al atoms are not homogeneously distributed throughout the zeolite lattice, or that there is a synergetic effect between the two Al atoms even when they are in different cages that would lead to stabilization of the divalent Pt^{2+} ion.

In order to rule out the possibility that Pt loading heterogeneity originated due to Pt redistribution during calcination and reduction treatments, we have also investigated a separate sample (IE-1.0) prior to these treatments, that is, after impregnation and drying (Supporting Information, Figure S3). The Pt–Al dependence for the dried sample was identical to that after the sample was calcined and reduced, confirming that the heterogeneity occurred in an earlier stage of the synthesis and that no significant amount of Pt is redistributed between crystals during calcination and reduction. Furthermore, it could be argued that difference in Pt loading was related to difference in mesopore volumes between zeolite crystals, and hence difference in Pt precursor diffusion. However, Figure 2 clearly demonstrates that despite comparable size and meso-pore density within, two zeolite crystals can have markedly different Pt loading, ruling out mesopore impact on the Pt diffusion.

While the origin of Pt loading heterogeneities can be clearly correlated to heterogeneities in Si/Al ratio between zeolite crystals, the origin of these Si/Al ratio heterogeneities between zeolite crystals is still to be understood. One of the possibilities
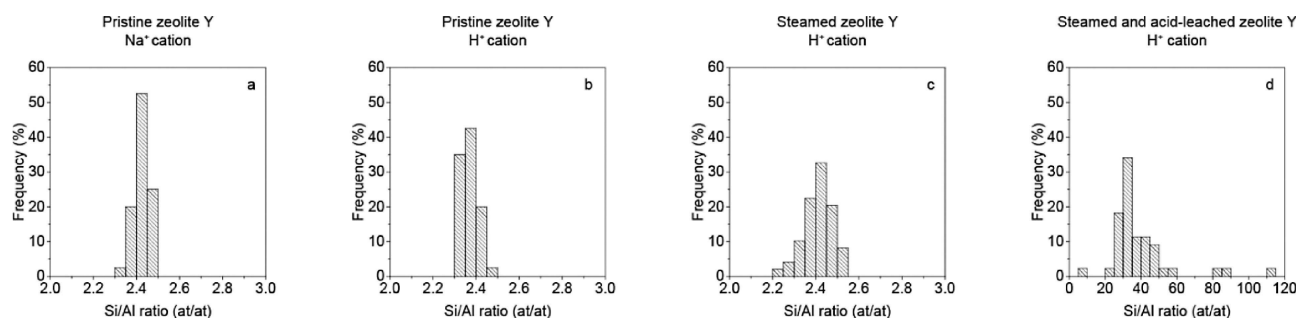
Figure 5. Quantitative EDX analysis of chemical compositions of individual zeolite Y crystals for different commercial zeolite Y supports. Histograms show the frequencies for the Si/Al ratio for pristine zeolite Na—Y (a), pristine zeolite H—Y (b), steamed zeolite H—Y (c) and steamed and acid leached zeolite H—Y (d).

is that this heterogeneity is introduced during the zeolite post-synthesis treatments, i. e. the steaming and/or acid leaching of pristine zeolite Y. For ZSM-5 zeolite crystals it is well known that Al-zoning, that is, regions with increased concentration of Al within individual zeolite crystals, can occur.[38–43] In order to verify whether Al zoning was also present in the zeolite Y samples used in this study, EDX elemental mapping of Si and Al was performed (Figure 4). For pristine zeolite Y (Zeolyst, CBV300) as well as steamed and acid leached zeolite Y (Zeolyst, CBV760), it can be seen that Si as well as Al are homogeneously distributed throughout the crystals. This is also well in line with the fact that no segregation of Pt was observed in this study, which confirms the close relationship between presence of Al and Pt.

Although no Al zoning was observed within individual zeolite crystals, quantitative EDX analysis of zeolite Y after different post-synthesis treatment steps showed that Si/Al ratio increasingly varies between crystals (Figure 5). In as synthesized Na-form of zeolite Y (Zeolyst, CBV100) most of the zeolite Na—Y crystals had comparable Si/Al ratios ranging from 2.3 to 2.5 with the majority of the crystals having Si/Al of 2.4 (Figure 5a), which is close to the reported value of 2.55, as given by the manufacturer. Subsequent treatment with ammonium (Zeolyst, CBV300) and calcination to transform zeolite NH$_4$—Y into H—Y zeolite, had minor impact on Si/Al ratio (Figure 5b). Steaming treatment (Zeolyst, CBV400) broadened the distribution of Si/Al ratios from 2.2 to 2.6, indicating difference in zeolite crystal's response to the steaming treatment (Figure 5c). When steamed zeolite Y is acid leached (Zeolyst, CBV760) significant variation in Si/Al ratios between crystals can be observed (Figure 5d).

While the average Si/Al ratio reported for this material is 30, EDX analysis shows very broad distribution of Si/Al from 20 to 50. It is argued in earlier research[24,44] that during the steaming step, hydrolysis of Si—O—Al bonds takes place and aluminum is expelled from the framework, leaving vacancies that are partly filled with mobile Si species and partly transformed into mesopores. Expelled aluminum remains in the mesopores as "extra-framework aluminum", and average Si/Al ratio remains the same as that of the parent zeolite material. Subsequent acid leaching, removes extra-framework aluminum species from mesopores, leaving the zeolite with a higher Si/Al ratio on average. Large differences in Si/Al ratio observed in our study,

suggest that individual zeolite crystals have different susceptibility to aluminum extractions which could be related to different amount of lattice defects within the crystals.[45] In view of the continuously advancing tools in electron microscopy and image analysis, we envisage that future studies will be able to further unravel the question of susceptibility of zeolite crystals to structural and chemical changes taking place during mesopore formation.

Conclusions

The importance of and the ability to control the nanoscale properties of catalysts is frequently addressed in literature, with focus being on establishing well dispersed metal nanoparticles. Metal location and local loading of the support, which can be equally essential for catalyst performance, are often overlooked. This study unravels variations in Pt loading between zeolite crystals in bifunctional Pt-zeolite Y catalysts, and links them to unexpected variations in Si/Al ratio between zeolite crystals. It was demonstrated that two commonly used metal deposition methods, incipient wetness impregnation and ion-exchange, were both sensitive to zeolite composition and unsuccessful in producing homogenously distributed metal particles across the support. Furthermore, it was demonstrated that the variation in zeolite composition likely occurs during zeolite post-synthesis treatments. In view of the great relevance of this and other zeolite-based catalysts in oil-refining industry, further investigations into the origin of such heterogeneities, and developing methods to suppress it, could potentially lead to further improvements of zeolite-based catalytic processes.

Experimental Section

Catalyst Synthesis

Catalyst were prepared with either incipient wetness impregnation (IWI) or ion-exchange (IE). For both methods four different catalysts were prepared with different weight loadings of platinum metal.

Ion-Exchange. 1 gram of ultra-stable zeolite Y (Zeolyst, CBV760) was dispersed in 200 mL milli-Q water and left to stir for an hour.

Platinum precursor, prepared by dissolving different amounts of Pt $(NH_3)_4(NO_3)_2$ in 20 mL milli-Q to prepare catalysts with Pt-loadings ranging from 1.3 to 2.4 wt% as listed in Table 1, was added dropwise. After the precursor addition, the dispersion was left to stir for 3 hours. Subsequently the sample was filtered over a Büchner filter and washed with 300 mL milli-Q to remove excess of Pt-precursor. The sample was dried for 3 hours at 60 °C in static air. Subsequently the sample was transferred to a muffle oven and dried overnight in static air at 120 °C.

Incipient Wetness Impregnation. 1 gram of ultra-stable zeolite Y (CBV760, Zeolyst) was dried overnight in a round bottom flask under vacuum. Subsequently, the amount of dried zeolite Y was weighed, after which the material was dried for 1 more hour under vacuum. The platinum precursor solution was prepared by dissolving different amounts of $Pt(NH_3)_4(NO_3)_2$ in demi-water. Taking into account zeolite Y pore volume, the corresponding precursor volume was taken up by a syringe to aim for a weight loading ranging from 0.9 to 2.8 wt%. Hereafter, the precursor solution was added dropwise to the dried zeolite Y, while stirring with a magnetic stirrer. It was aimed to fill up 90 % of the zeolite Y pore volume, which was 0.4 cm³/g as determined with N_2-physisorption. The impregnated powder was left to stir for another 30 minutes. The sample was then transferred into an oven and dried for 3 hours at 60 °C in static air. Subsequently the sample was transferred to a muffle oven and dried overnight at 120 °C in static air.

Calcination and reduction. Prior to calcination and reduction, all samples were pressed into a tablet, crushed and sieved into a particle size fraction of 212–500 μm. Subsequently, 0.26 gram of the sieved fraction was loaded into a quartz reactor. Calcination was performed at 300 °C (ramp 0.2 °C/min) for 30 minutes under airflow (GHSV = 2600 h⁻¹). The sample was cooled down to room temperature and the reactor was flushed with N_2 for 30 minutes. Without disconnecting the reactor, the reduction was performed at 300 °C (ramp 1.0 °C/min) for 1 hour under pure H_2 flow (GHSV = 2600 h⁻¹). Thereafter the sample was cooled down to room temperature and stored for further use.

Characterization

Transmission electron microscopy (TEM) measurements were performed on a Talos F200X (FEI) microscope equipped with an X-FEG electron source and a Super-X™ EDX detector. The microscope was operated at 200 kV. Scanning transmission electron microscopy (STEM) images were acquired with a frame time of 20 seconds. Averaged particle sizes were determined by measuring at least 500 metal nanoparticles for each sample. Surface averaged particle sizes were determined by using the following formula:
$$d_s = \sqrt{\left(\frac{1}{N}\sum_{N=1}^{N} d_i^2\right)}$$
where d_s is the surface averaged particle size, d_i is the number averaged diameter of the individual particles and N is the total number of particles counted.

Energy dispersive X-ray spectroscopy (EDX) measurements were performed in transmission electron microscopy (TEM) mode. TEM-EDX spectra to determine the bulk elemental composition of Pt-zeolite catalysts were obtained by spreading the electron beam across tens of micrometers regions containing large aggregates of Pt-zeolite crystals. Spectra were acquired in TIA software (FEI) with 5 minutes acquisition time. The Pt loading of a sample was calculated by averaging elemental composition derived from 5 different regions. Single crystal TEM-EDX spectra were obtained by spreading the electron beam around one Pt-zeolite crystal at a time, making sure no other material was irradiated by the electron beam. Spectra were collected with 10 minutes acquisition time using TIA. Quantification of spectra for bulk as well as single crystal measurements was performed in ES Vision software. A background correction was performed manually, while peak identification was performed automatically by the software. Subsequently quantification to atomic ratios was performed with the Cliff-Lorimer technique. The results of these individual zeolite EDX quantifications were visualized in graphs where the Pt/(Si + Al) atomic ratio was plotted versus the Al/(Si + Al) atomic ratio. Finally, the results were fitted with a linear function, $y = a + bx$ where a (intercept) and b (slope) are variables (Supporting Information, Table S1), in order to fit the obtained results as optimally as possible.

TEM-EDX elemental maps of 2048×2048 pixels were acquired with 5 minutes acquisition time using Velox software.

Scanning electron microscopy (SEM) EDX measurements were performed on a XL30sfeg, equipped with an EDAX super ultrathin window detector. The microscope was operated at 25 kV. EDX spectra were acquired with 10 minutes acquisition time using EDAX software, and scanning regions were 1600 μm² in size containing large aggregates of Pt-zeolite crystals. A manual background correction was performed, the areas of the different peaks were obtained and the results were quantified. To derive bulk Pt loading of a sample, 6 different regions were analyzed with SEM-EDX, spectra were quantified and the results were averaged.

Hydrogen chemisorption measurements were performed on a Micromeritics ASAP 2020C instrument. Samples were reduced at 300 °C in flowing H_2 for 1 h and subsequently evacuated at 300 °C. The H_2 uptake was measured at 35 °C. For the calculations (hemi) spherical particles, an $H:Pt_s$ stoichiometry of 1 and an atomic cross section of Pt of 0.08 nm² were assumed.

X-ray diffraction diffractograms were recorded on a Bruker-AXS D2 Phaser X-ray Diffractometer in Bragg-Brentano mode, equipped with a Lynxeye detector (Co $K_{\alpha 1,2}$, $\lambda = 1.790$ Å). Recordings were taken between 6° and 60° 2θ, under constant rotation of 15 rpm. Prior to the measurements, samples were crushed into a fine powder.

Conflict of Interest

The authors declare no conflict of interest.

[1] M. A. Arribas, A. Martínez, *Appl. Catal. A* **2002**, *230*, 203–217.
[2] K. C. Park, S. K. Ihm, *Appl. Catal. A* **2000**, *203*, 201–209.
[3] A. Patrigeon, E. Benazzi, C. Travers, J. Y. Bernhard, *Catal. Today* **2001**, *65*, 149–155.
[4] G. G. Martens, G. B. Marin, J. A. Martens, P. A. Jacobs, G. V. Baron, *J. Catal.* **2000**, *195*, 253–267.
[5] J. Weitkamp, *ChemCatChem* **2012**, *4*, 292–306.

[6] J. Zečević, G. Vanbutsele, K. P. de Jong, J. A. Martens, *Nature* **2015**, *528*, 245–254.

[7] F. Alvarez, F. R. Ribeiro, G. Perot, C. Thomazeau, M. Guisnet, *J. Catal.* **1996**, *162*, 179–189.

[8] J. de Graaf, A. J. van Dillen, K. P. de Jong, D. C. Koningsberger, *J. Catal.* **2001**, *203*, 307–321.

[9] G. Prieto, J. Zečević, H. Friedrich, K. P. de Jong, P. E. de Jongh, *Nat. Mater.* **2013**, *12*, 34–39.

[10] P. B. Weisz, *Adv. Catal.* **1962**, *13*, 137–190.

[11] J. Francis, E. Guillon, N. Bats, C. Pichon, A. Corma, L. J. Simon, *Appl. Catal. A* **2011**, *409–410*, 140–147.

[12] E. Blomsma, J. A. Martens, P. A. Jacobs, *J. Catal.* **1997**, *165*, 241–248.

[13] G. Kinger, H. Vinek, *Appl. Catal. A* **2001**, *218*, 139–149.

[14] M. Guisnet, F. Alvarez, G. Giannetto, G. Perot, *Catal. Today* **1987**, *1*, 415–433.

[15] M. Guisnet, *Catal. Today* **2013**, *218–219*, 123–134.

[16] W. Vermeiren, J. P. Gilson, *Top. Catal.* **2009**, *52*, 1131–1161.

[17] H. Deldari, *Appl. Catal. A* **2005**, *293*, 1–10.

[18] K. P. de Jong, J. Zečević, H. Friedrich, P. E. de Jongh, M. Bulut, S. van Donk, R. Kenmogne, A. Finiels, V. Hulea, F. Fajula, *Angew. Chem. Int. Ed.* **2010**, *49*, 10074–10078.

[19] J. Pérez-Ramírez, C. H. Christensen, K. Egeblad, C. H. Christensen, J. C. Groen, *Chem. Soc. Rev.* **2008**, *37*, 2530–2542.

[20] K. Li, J. Valla, J. Garcia-Martinez, *ChemCatChem* **2014**, *6*, 46–66.

[21] J. L. Agudelo, E. J. M. Hensen, S. A. Giraldo, L. J. Hoyos, *Fuel Process. Technol.* **2015**, *133*, 89–96.

[22] D. Verboekend, N. Nuttens, R. Locus, J. van Aelst, P. Verolme, J. Pérez-Ramírez, B. F. Sels, *Chem. Soc. Rev.* **2016**, *45*, 3331–3352.

[23] Y. Tao, H. Kanoh, L. Abrams, K. Kaneko, *Chem. Rev.* **2006**, *106*, 896–910.

[24] S. van Donk, A. H. Janssen, J. H. Bitter, K. P. de Jong, *Catal. Rev. Sci. Eng.* **2003**, *45*, 297–319.

[25] A. H. Janssen, A. J. Koster, K. P. de Jong, *Angew. Chem. Int. Ed.* **2001**, *113*, 1136–1138.

[26] P. Munnik, P. E. de Jongh, K. P. de Jong, *Chem. Rev.* **2015**, *115*, 6687–6718.

[27] B. M. Weckhuysen, *Angew. Chem. Int. Ed.* **2009**, *48*, 4910–4943.

[28] L. Espinosa-Alonso, K. P. de Jong, B. M. Weckhuysen, *Phys. Chem. Chem. Phys.* **2010**, *12*, 97–107.

[29] E. Plessers, I. Stassen, S. P. Sree, K. P. F. Janssen, H. Yuan, J. Martens, J. Hofkens, D. de Vos, M. B. J. Roeffaers, *ACS Catal.* **2015**, *5*, 6690–6695.

[30] E. Plessers, J. E. van den Reijen, P. E. de Jongh, K. P. de Jong, M. B. J. Roeffaers, *ChemCatChem* **2017**, *9*, 4562–4569.

[31] J. Zečević, A. M. J. van der Eerden, H. Friedrich, P. E. de Jongh, K. P. de Jong, *ACS Nano* **2013**, *7*, 3698–3705.

[32] K. P. de Jong, J. Zečević, *Nat. Mater.* **2016**, *16*, 7–8.

[33] B. J. Kip, F. B. M. Duivenvoorden, D. C. Koningsberger, R. Prins, *J. Catal.* **1987**, *105*, 26–38.

[34] J. Dědeček, Z. Sobalík, B. Wichterlová, *Catal. Rev. Sci. Eng.* **2012**, *54*, 135–223.

[35] M. J. Remy, D. Stanica, G. Poncelet, E. J. P. Feijen, P. J. Grobet, J. A. Martens, P. A. Jacobs, *J. Phys. Chem.* **1996**, *100*, 12440–12447.

[36] A. Boréave, A. Auroux, C. Guimon, *Microporous Mater.* **1997**, *11*, 275–291.

[37] A. S. Andreev, V. Livadaris, *J. Phys. Chem. C* **2017**, *121*, 14108–14119.

[38] R. Althoff, B. Schulz-Dobrick, F. Schüth, K. Unger, *Microporous Mater.* **1993**, *1*, 207–218.

[39] R. von Ballmoos, W. M. Meier, *Nature* **1981**, *289*, 782–783.

[40] E. G. Derouane, S. Detremmerie, Z. Gabelica, N. Blom, *Appl. Catal.* **1981**, *1*, 201–224.

[41] N. Danilina, F. Krumeich, S. A. Castelanelli, J. A. Van Bokhoven, *J. Phys. Chem. C* **2010**, *114*, 6640–6645.

[42] Z. Ristanović, J. P. Hofmann, U. Deka, T. U. Schülli, M. Rohnke, A. M. Beale, B. M. Weckhuysen, *Angew. Chem. Int. Ed.* **2013**, *52*, 13382–13386.

[43] D. E. Perea, I. Arslan, J. Liu, Z. Ristanović, L. Kovarik, B. W. Arey, J. A. Lercher, S. R. Bare, B. M. Weckhuysen, *Nat. Commun.* **2015**, *6*, 1–8.

[44] C. R. Marcilly, *Pet. Tech.* **1986**, *328*, 12–18.

[45] Y. Sasaki, T. Suzuki, Y. Takamura, A. Saji, H. Saka, *J. Catal.* **1998**, *178*, 94–100.